A Methodology for Measuring Cirrus Cloud Visible-to-Infrared Spectral Optical Depth Ratios

DANIEL H. DESLOVER AND WILLIAM L. SMITH*

Cooperative Institute for Meteorological Satellite Studies, Space Science and Engineering Center, University of Wisconsin—Madison, Madison, Wisconsin

PAIVI K. PIIRONEN+ AND EDWIN W. ELORANTA

Space Science and Engineering Center, University of Wisconsin—Madison, Madison, Wisconsin

(Manuscript received 2 June 1997, in final form 20 February 1998)

ABSTRACT

Knowledge of cirrus cloud optical depths is necessary to understand the earth's current climate and to model the cloud radiation impact on future climate. Cirrus clouds, depending on the ratio of their shortwave ''visible'' to longwave ''infrared'' optical depth, can act to either cool or warm the planet. In this study, visible-to-infrared cirrus cloud optical depth ratios were measured using ground-based lidar and Fourier transform spectrometry. A radiosonde temperature profile combined with the 0.532-μm-high spectral resolution lidar vertical cloud optical depth profile provided an effective weighting to the cloud radiance measured by the interferometer. This allowed evaluation of cirrus cloud optical depths in 18 infrared microwindows between water vapor absorption lines within the 800–1200-cm^{-1} infrared atmospheric window. The data analysis was performed near the peak solar and terrestrial emission regions, which represent the effective radiative cloud forcing efficiency of the given cloud sample. Results are also presented that demonstrate the measurement of infrared optical depth using an assumed uniform cloud extinction cross section, which requires generic lidar cloud boundary data. The measured cloud extinction profile provided a more robust solution that would allow analysis of multiple-layer clouds and removed the uniform cloud extinction cross-section assumption. Mie calculations for ice particles were used to generate visible and infrared extinction coefficients; these were compared against the measured visible-to-infrared optical depth ratios. The results demonstrate strong particle size and shape sensitivity across the infrared atmospheric window.

1. Introduction

The climatic importance of atmospheric anthropogenic gases such as carbon dioxide and methane, in addition to the state of the ozone layer, is currently a major scientific and political issue (Schneider 1990; Chappelaz et al. 1993; Genthon et al. 1987). Cirrus clouds play a climatic role similar to that of the ''greenhouse gases.'' Studies have shown that both natural (Prabhakara et al. 1993) and anthropogenic (Smith et al. 1998) cirrus can produce a greenhouse warming effect.

Recent technological advancement has enabled the measurement of visible and infrared cloud radiative properties using both ground-based and spaceborne instrumentation incorporating active and passive remote sensing techniques (Rossow and Lacis 1990; Ackerman et al. 1993). This paper introduces a novel approach to measure cirrus cloud visible-to-infrared optical depth ratios for the infrared longwave atmospheric window (800–1200 cm^{-1}). The methodology requires simultaneous active and passive high spectral resolution cloud remote sensing measurements. The instruments used to make these measurements were the Atmospheric Emitted Radiance Interferometer (AERI) (Smith et al. 1995), the High Spectral Resolution Lidar (HSRL) (Piironen and Eloranta 1994), and the Cross-Chain Loran Atmospheric Sounding System (CLASS). The AERI and HSRL are ground-based, near-zenith viewing instruments that observe a vertical atmospheric column advected into the instrument's respective field of view (FOV). The CLASS is a radiosonde system that provides atmospheric state information required to interpret the AERI and HSRL data. Section 2 provides a brief overview of the AERI and HSRL systems.

The use of simultaneous active and passive measurements to derive cirrus cloud optical properties is not new. Platt (1973) measured simultaneous visible and infrared cirrus optical properties using a ground-based

* Current affiliation: NASA/Langley Research Center, Hampton, Virginia.
+ Current affiliation: Vaisala Oy, Helsinki, Finland.

Corresponding author address: Daniel H. DeSlover, CIMSS, Space Science and Engineering Center, University of Wisconsin—Madison, 1225 W. Dayton St., Madison, WI 53706.
E-mail: deslover@ssec.wisc.edu

visible single-channel lidar and a broadband radiometer. Our approach enhances Platt's method by incorporating high spectral remote sensing of both visible and infrared radiation. The HSRL offers a calibrated return signal, yielding a true vertical aerosol optical depth profile at 0.532 μm. High-spectral-resolution AERI measurements in the infrared provide the unique opportunity to observe cirrus cloud radiative properties between water vapor lines in the least contaminated regions of the infrared atmospheric window. The high spectral resolution also offers an increase in the number of infrared data points, which allows measurement of spectral variation while reducing the overall error due to water vapor absorption lines.

Two approaches are offered that take advantage of the high spectral resolution AERI radiance measurements. The first technique assumes a single-layer cloud of uniform extinction cross section. Lidar measurements supply only cloud-base and cloud-top altitude data such that the radiative transfer equation is inverted to derive the cloud optical depth for each spectral microwindow. Section 3 will discuss the radiative transfer equation, while the inversion process is detailed in section 4. Results obtained with this approach are illustrated in section 7a. The second technique, described in section 5, uses the unique capability of the HSRL, which measures the visible aerosol optical depth profile. Section 6 demonstrates how the radiative transfer equation is solved in a forward calculation while iterating the visible optical depth by a scale factor, $\alpha(\nu)^{-1}$, for each AERI spectral ''microwindow.'' The resultant iterated values of $\alpha(\nu)$, as shown in section 7b, represent a spectrum of visible-to-infrared optical depth ratios across the atmospheric infrared window. The scale factor $\alpha(\nu)$ is derived from data near the peak of both downwelling solar radiation (lidar wavelength) and upwelling terrestrial radiation (infrared microwindows); thus, it provides a mechanism for measuring the effective cloud forcing in a spectral region that is nearly transparent without a cloud cover. Use of the HSRL optical depth profile also removes the assumption of a uniform cloud extinction cross section and allows measurements for multiple-layer clouds.

The results in section 7b are also compared with calculations using the Mie theory. Both particle size and shape sensitivity are apparent in the data due to a transition from strong to weak ice absorption between 800 and 1200 cm^{-1}. Regions of weak ice absorption (950–1200 cm^{-1}) demonstrated the sensitivity to particle shape. It will be shown that the clouds examined in this paper consisted of roughly 50-μm effective radius particles.

Data were acquired at the University of Wisconsin—Madison during simultaneous operation of the HSRL and AERI systems in winter conditions. The two cases presented in this paper were chosen due to their variability in both optical and geometrical cloud thickness for ice-phase clouds. The continuation of these measurements and analysis using the methodology presented here will produce a cloud radiation property climatology that can be used to parameterize the cirrus cloud radiative heating process in general circulation models (GCMs). The parameterization might be in the form of regression equations that relate radiative flux divergence to cloud optical thickness, geometrical thickness, particle effective radius, altitude, temperature, and general synoptic environment.

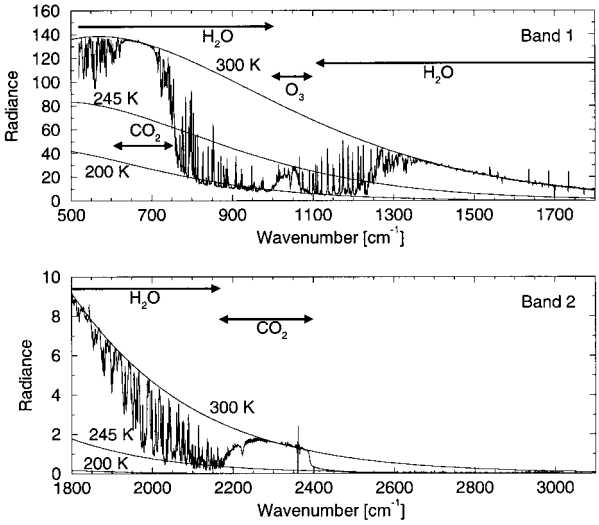

FIG. 1. Illustration of atmospheric downwelling band 1 (upper) and band 2 (lower) AERI radiance relative to values derived from the Planck function for various temperatures. Also noted are the absorption regions for various atmospheric constituents. The spikes in the measured radiance, between 1500 and 1800 cm^{-1} in band 1 and near 2360 cm^{-1} in band 2, are a result of water vapor and carbon dioxide absorption lines, respectively, which become opaque within the instrument.

2. Instrumentation

a. Atmospheric Emitted Radiance Interferometer

The AERI obtained downwelling atmospheric emission spectra at wavenumbers between 520 and 3020 cm^{-1} (3.3–19.2-μm wavelength) with an unapodized spectral resolution of 0.5 cm^{-1}. Data are combined from two bands, band 1 and band 2, which cover 520–1800 cm^{-1} and 1800–3020 cm^{-1}, respectively. The AERI full-angle FOV is 32 mrad.

The system alternates between three viewing modes: ambient blackbody calibration reference (1.5 min), 60°C hot blackbody calibration reference (1.5 min), and zenith atmospheric view (3 min). Including data transfer time, a data sample frequency of 6.2 min is achieved. The dwell times are specific to this experiment, where the standard instrument dwell times were reduced by 33% to increase the AERI temporal resolution to facilitate comparison with the lidar data. More detailed descriptions of the AERI instrument are given by Smith et al. (1995).

Figure 1 illustrates AERI-measured downwelling spectral radiance for both band 1 (upper plot) and band

2 (lower plot). Band 1 microwindow data are used in the data analysis; band 2 data are shown for completeness. The dominant species are CO_2 [600–800 cm^{-1} (15 μm) and 2200–2400 cm^{-1} (4.3 μm)], O_3 [1000–1060 cm^{-1} (9.6 μm)], and H_2O. The opaque CO_2 and H_2O absorption features follow the spectral distribution of the Planck radiance corresponding to the surface air temperature of about 297 K. The atmospheric window (800–1200 cm^{-1}) is the most transparent region in the spectrum. Measurements between water vapor lines within the atmospheric window (referred to as microwindows and tabulated in appendix A) yield observations with the least atmospheric contamination.

b. High spectral resolution lidar system

Visible data are acquired with the 0.532-μm HSRL in a 160-μrad full-angle FOV. The HSRL provided calibrated vertical profiles of aerosol backscatter cross section, optical depth, and backscatter depolarization in the near-zenith direction. A 4° offset from the vertical prevents specular reflection from horizontally oriented crystals in cirrus clouds. HSRL data are acquired with 15-m vertical resolution using a 4-kHz laser repetition rate. Data points are stored in 4000-shot averages. Piironen (1994) gives a complete HSRL system description.

Backscatter depolarization discriminates between spherical and nonspherical particles. Spherical particles backscatter photons with a small change in the depolarization, where a zero depolarization implies no change in the degree of polarization. Nonspherical particle backscatter (e.g., ice crystals, dust) partially depolarizes the return signal. Range-resolved measurements of depolarization provide analysis of cloud phase and distinguish spherical and nonspherical boundary-layer aerosols. Separation of the aerosol and molecular backscattered energy is a unique HSRL characteristic, which is accomplished with a narrowband iodine absorption filter (Piironen and Eloranta 1994). This separation allows unambiguous measurement of aerosol and molecular backscatter.

The lower plot of Fig. 2 illustrates the HSRL-measured aerosol and molecular backscattered return as a function of altitude. The column-integrated visible optical depth, shown in the upper plot, is due to aerosol attenuation of the molecular signal. Aerosol backscatter, represented by the dashed curve, increases inside cloud layers (5.5–7.5 km) and the haze layer (3.5–5 km). The optical depth is theoretically a monotonic function of range. Uncertainty in the aerosol optical depth beyond cloud top is due to photon counting errors in the lidar data, where the uncertainty approaches infinity as the cloud becomes opaque (i.e., no photons return). The error in the column optical depth is consistent with the uncertainty shown in adjacent range bins.

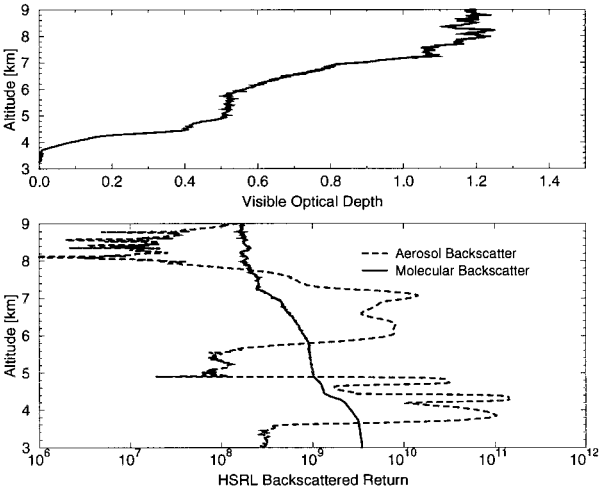

FIG. 2. Upper plot illustrates HSRL-measured column-integrated visible optical depth relative to inverted aerosol (dashed line) and molecular (solid line) backscatter returns are shown in the lower plot.

3. Infrared radiance

The radiative transfer equation (RTE) for downwelling spectral radiance in a cloudy atmosphere, assuming a single cloud layer, can be partitioned into layers: clear sky below the cloud, the cloud layer, and clear sky above the cloud. It is described by the relation

$$
\begin{aligned}
R(\nu)\downarrow \approx & \int_{p_b}^{p_s} B[\nu, T(p)]\, d\tau_{\mathrm{clr}}(\nu, p, p_s) + \tau_{\mathrm{clr}}(\nu, p_b, p_s) \\
& \times \left(\int_{p_t}^{p_b} B[\nu, T(p)]\, d[\tau_{\mathrm{clr}}(\nu, p, p_b)\tau_{\mathrm{cld}}(\nu, p, p_b)] \right. \\
& + \tau_{\mathrm{clr}}(\nu, p_t, p_b)\tau_{\mathrm{cld}}(\nu, p_t, p_b) \int_{0}^{p_t} B[\nu, T(p)]\, d\tau_{\mathrm{clr}}(\nu, p, p_t) \\
& \left. + r(\nu, \tau_{\mathrm{cld}}) \left[B(\nu, T_s)\tau_{\mathrm{clr}}(\nu, p_b, p_s) + \int_{p_s}^{p_b} B[\nu, T(p)]\, d\tau_{\mathrm{clr}}(\nu, p, p_b) \right] \right), \qquad (1)
\end{aligned}
$$

where $R(\nu)\downarrow$ is the downwelling column radiance; $B[\nu, T(p)]$ is the Planck radiance; and $\tau_{\rm clr}(\nu, p, p_i)$ [$\tau_{\rm cld}(\nu, p, p_i)$] is the clear- (cloudy-) sky transmissivity of the atmosphere bounded by the pressure levels p_i and p. The variables p_s, p_b, p_t, and 0 represent surface, cloud base, cloud top, and top of atmosphere pressures, respectively. The term $r(\nu, \tau_{\rm cld})$ is the angular integrated cloud reflectance divided by π, assuming a diffusely reflective cloud. The radiance is expressed in milliwatts $(\text{m}^2\ \text{sr}\ \text{cm}^{-1})^{-1}$. Only molecular absorption between water vapor absorption lines is considered. Therefore, the radiance contribution from the cirrus cloud top to the top of atmosphere is negligible and ignored.

The first three terms of Eq. (1) are the downwelling components from the various atmospheric layers, while the last term accounts for the reflection of upwelling terrestrial and atmospheric radiation from below the cloud. The clear-sky radiance and transmission components, representing the gaseous atmosphere, are determined using the Line-by-Line Radiative Transfer Model (LBLRTM) (Clough et al. 1992). Cloud reflectance is based on a parameterization for 50-μm ice spheres, as described herein.

a. LBLRTM

LBLRTM is required to determine downwelling clear-sky radiance below the cloud base [Eq. (2)]; upwelling clear-sky radiance, including the terrestrial contribution, below the cloud base [Eq. (3)]; and clear-sky transmission below the cloud base [Eq. (4)]:

$$R_{\rm clr}^{\rm LBL}(\nu, p_s, p_b)\downarrow = \int_{p_b}^{p_s} B[\nu, T(p)]\, d\tau_{\rm clr}(\nu, p, p_s), \quad (2)$$

$$R_{\rm clr}^{\rm LBL}(\nu, p_s, p_b)\uparrow = B(\nu, T_s)\tau_{\rm clr}(\nu, p_b, p_s) + \int_{p_s}^{p_b} B[\nu, T(p)]\, d\tau_{\rm clr}(\nu, p, p_b), \quad (3)$$

$$\tau_{\rm clr}^{\rm LBL}(\nu, p_s, p_b) = \tau_{\rm clr}(\nu, p_b, p_s). \quad (4)$$

A local radiosonde measurement provides the temperature and water vapor profiles required for the LBLRTM calculations.

b. Cloud reflectivity

Model simulations using an adding–doubling model (Collard et al. 1995), incorporating Mie theory phase functions, show that the cirrus scattered upwelling infrared radiance received at the surface is at least two orders of magnitude smaller than cloud emission. The Mie theory phase functions are derived using a 50-μm-radius (0.25 variance) gamma size distribution (Hansen 1971), assuming spherical particles and using the index of refraction for ice (Warren 1984). This size choice is consistent with in situ measurements of naturally occurring cirrus (Francis, 1995).

The cloud reflectance will vary for each microwindow because of the spectral dependent index of refraction for ice water. It will also depend on the cloud transmissivity, which cannot be inverted from the RTE until the reflectance is known. Therefore, an iterative solution is necessary and requires parameterizing the reflectance as a function of cloud transmissivity, $r(\nu, \tau_{\rm cld})$. The reflectance is determined with the adding–doubling model by monitoring the ratio of upwelling relative to downwelling radiant flux at the cloud base. This approach is feasible if a particle size distribution is assumed and if each microwindow region is independently parameterized. The technique is outlined for a sample AERI microwindow wavenumber in appendix B.

4. Infrared optical depth

The infrared cirrus cloud optical depth in each spectral microwindow can be determined by inverting the RTE using the AERI-measured downwelling radiance if one assumes a uniform extinction cross section between lidar-measured cloud-base and cloud-top altitudes. The infrared optical depths are derived by using an atmospheric transmission model to calculate the clear-sky radiance and transmissivity in each microwindow given a local radiosonde profile, where the remaining column radiance is due to cloud emission.

Equation (1) is now given in terms of the AERI-measured radiance and LBLRTM parameters for a cloud with uniform extinction cross section between boundaries p_b and p_t, and using Eqs. (2)–(4):

$$R_m\downarrow \approx R_{\rm clr}^{\rm LBL}(p_s, p_b)\downarrow + r(\tau_{\rm cld})\tau_{\rm clr}^{\rm LBL}(p_s, p_b) \times R_{\rm clr}^{\rm LBL}(p_s, p_b)\uparrow + \tau_{\rm clr}^{\rm LBL}(p_s, p_b) \times \int_{p_t}^{p_b} B[\nu, T(p)]\, d[\tau_{\rm clr}(p, p_b)\tau_{\rm cld}(p, p_b)], \quad (5)$$

where the radiance contribution above the high cirrus cloud is assumed to be negligible and spectral dependence is implied. Rearranging terms results in a radiance value that effectively projects the instrument to cloud base:

$$\int_{p_t}^{p_b} B[T(p)]\, d[\tau_{\rm clr}(p, p_b)\tau_{\rm cld}(p, p_b)] \approx \frac{R_m\downarrow - R_{\rm clr}^{\rm LBL}(p_s, p_b)\downarrow - r(\tau_{\rm cld})\tau_{\rm clr}^{\rm LBL}(p_s, p_b)R_{\rm clr}^{\rm LBL}(p_s, p_b)\uparrow}{\tau_{\rm clr}^{\rm LBL}(p_s, p_b)}.$$

Integration by parts transforms the left-hand side into

$$\left\{B[T(p)]\tau_{\rm clr}(p,\,p_b)\tau_{\rm cld}(p,\,p_b)\right\}\Big|_{p_t}^{p_b} - \int_{p_t}^{p_b}\tau_{\rm clr}(p,\,p_b)\tau_{\rm cld}(p,\,p_b)\,dB[T(p)].$$

The trapezoid rule is applied to the remaining integral at the endpoints to obtain a final solution for the cloud transmissivity:

$$\tau_{\rm cld}(p_t,p_b)\approx\frac{1}{\tau_{\rm clr}^{\rm LBL}(p_t,p_b)}\left[1-\frac{R_{\rm cld}(\tau_{\rm cld},p_s,p_b,p_t)\downarrow}{\tau_{\rm clr}^{\rm LBL}(p_s,p_b)B_{\rm mid\_cld}}\right],\quad(6)$$

where

$$R_{\rm cld}(\tau_{\rm cld},p_s,p_b,p_t)\downarrow = R_m\downarrow - R_{\rm clr}^{\rm LBL}(p_s,p_b)\downarrow - r(\tau_{\rm cld})\tau_{\rm clr}^{\rm LBL}(p_t,p_b)R_{\rm clr}^{\rm LBL}(p_s,p_b)\uparrow$$

is the downwelling cloud radiance and

$$B_{\rm mid\_cld}=\frac{B[T(p_b)]+B[T(p_t)]}{2}$$

is the average Planck radiance of the cloud determined from local radiosonde data and lidar-measured cloud boundaries. The clear-sky transmissivity within the cloud, $\tau(\nu,\,p_t,\,p_b)$, is obtained from LBLRTM. The solution is iterated for $\tau_{\rm cld}$ in the reflectance term until a solution converges to within 0.001 mW $(\mathrm{m^2\ sr\ cm^{-1}})^{-1}$ (Ackerman et al. 1990).

The algorithm takes into consideration the fact that the cloud may be opaque. This reduces the effective cloud-top altitude while increasing the effective cloud-top temperature. Without this consideration, Eq. (6) would yield an unphysical solution based on true cloud-base and cloud-top temperatures. Therefore, a direct solution of Eq. (6) is not attempted because the measured radiance for an opaque cloud will be larger than the midcloud radiance determined from radiosonde measurements. The result is a $R_{\rm cld}\downarrow$:$B_{\rm mid\_cld}$ ratio that becomes larger than unity, yielding an unphysical (negative) transmittance solution of Eq. (6).

Instead, the cloud is broken into layers defined by the LBLRTM atmospheric levels, in which the cloud transmittance is calculated from the cloud base to a given altitude layer. If the transmittance becomes negative, the cloud is labeled as opaque at the previous altitude. Otherwise, the process continues until the cloud top is reached, where the solution is taken to be the cloud infrared transmittance. It will be shown that a cloud transmittance less than 0.05 (an infrared optical depth greater than 3) is the minimum resolvable value. The infrared cloud optical depth, $\delta_{\rm IR}(\nu)$, is related to the infrared cloud transmissivity by this relation: $\tau_{\rm cld}(\nu)=\exp[-\delta_{\rm IR}(\nu)]$.

Note that $\delta_{\rm IR}(\nu)$ does not include the molecular clear-sky portion of the atmosphere in which the cloud resides [i.e., $\delta_{\rm IR}(\nu)$ is only the cloud aerosol optical depth]. However, the molecular optical depth at this altitude is near zero (i.e., much less than 1% of the total measured microwindow radiance originates near cloud altitude). The infrared cloud optical depths are often compared to HSRL-measured visible optical depths, which are a direct measurement of the aerosol optical depth.

5. HSRL data

The range-resolved lidar power can be represented as (Grund and Eloranta 1991)

$$P(r)=E_0\frac{cA}{2r^2}\left[\frac{3}{8\pi}\beta_m(r)+\frac{p(\pi,\,r)}{4\pi}\beta_a(r)\right]\times\exp\left[-2\int_0^r\beta_\epsilon(r')\,dr'\right]+M(r)+b,\quad(7)$$

where $P(r)$ is the lidar power incident on the receiver from range r (W), E_0 is the laser pulse energy (J), c is the speed of light (m $\mathrm{s^{-1}}$), A is the receiver area ($\mathrm{m^2}$), $\beta_a(r)$ is the aerosol scattering cross section per unit volume from range r ($\mathrm{m^{-1}}$), $\beta_m(r)$ is the molecular scattering cross section per unit volume from range r ($\mathrm{m^{-1}}$), $\beta_\epsilon(r')$ is the extinction cross section per unit volume from range r ($\mathrm{m^{-1}}$), $3/(8\pi)$ is the Rayleigh molecular backscatter phase function ($\mathrm{sr^{-1}}$), $p(\pi,\,r)/(4\pi)$ is the aerosol backscatter phase function from range r ($\mathrm{sr^{-1}}$), $M(r)$ is the multiply scattered return power received from range r (W), and b is the background signal (W).

Direct measurement of optical depth is not possible with a single-channel lidar because of the inherent coupling of the extinction cross section with the aerosol and molecular backscatter cross sections. However, it can be accomplished with the separation of the return signal into the individual molecular and aerosol equations:

$$P_m(r)=E_0\frac{cA}{2r^2}\frac{3}{8\pi}\beta_m(r)\exp[-2\delta_{\rm vis}(r)]\quad(8)$$

and

$$P_a(r)=E_0\frac{cA}{2r^2}\frac{p(\pi,\,r)}{4\pi}\beta_a(r)\exp[-2\delta_{\rm vis}(r)],\quad(9)$$

respectively, where $\delta_{\rm vis}(r)=\int_0^r\beta_\epsilon(r')\,dr'$, the background contribution has been subtracted, and multiple scattering is assumed to be negligible. Multiple scattering is reduced in the HSRL return signal by reducing the detector field of view to 160 μrad. For the cases given in this paper, as much as 20% of the aerosol signal is due to multiply-scattered return. However, the overall effect on the optical depth profile is a redistribution of the optical depth to further range bins. The column optical depth is correct to within 3% by integrating just beyond cloud top (500 m) (Eloranta 1998). In this context, in which the radiance is calculated from the optical

depth profile, the radiance error is small, given the small temperature gradient near the cloud top.

The direct solution of aerosol extinction from Eq. (8) is possible because the spectral distribution of energy scattered by atmospheric molecules and aerosols depends upon their velocity. Molecules move with a mean velocity proportional to $\sqrt{T}$ in a distribution represented by Maxwellian statistics, where T is the temperature. Photons scattered from a molecule will have their energy shifted, resulting in a symmetric Doppler spectral broadening of the return signal relative to the transmitted light. However, much larger and slower moving aerosols have a velocity corresponding to the mean wind. Therefore, aerosol backscatter exhibits negligible spectral broadening for a pulse propagating in the zenith direction. The HSRL data allow separation of the molecular and aerosol signals based on this difference (Piironen and Eloranta 1994).

Separation of Eq. (7) into Eqs. (8) and (9) allows solution of various atmospheric properties. The molecular backscatter cross section per unit volume, $3/(8\pi)\beta_m(r)$, is

$$\frac{3}{8\pi}\beta_m(r) = 3.78 \times 10^{-6}\frac{p(r)}{T(r)} \tag{10}$$

at the laser wavelength of 0.532 μm (Measures 1992), where $p(r)$ and $T(r)$ are atmospheric pressure and temperature, respectively, at the lidar range, r. A local radiosonde provides the vertical temperature and pressure profiles. The molecular backscatter cross section per unit volume yields a calibration target for the lidar that is available at all ranges.

Substitution of $\beta_m(r)$ into Eq. (8) for two atmospheric levels r_1 and r_2 gives the optical depth of that layer at the lidar wavelength:

$$\delta_{\text{vis}} = \delta(r_2) - \delta(r_1) = \frac{1}{2}\ln\left[\frac{P_m(r_1)r_1^2\beta_m(r_2)}{P_m(r_2)r_2^2\beta_m(r_1)}\right]$$
$$= \frac{1}{2}\ln\left[\frac{P_m(r_1)r_1^2p(r_1)T(r_2)}{P_m(r_2)r_2^2p(r_2)T(r_1)}\right]. \tag{11}$$

6. Visible-to-IR optical depth ratio

One can apply the HSRL-measured visible optical depth profile discussed in section 5 to the radiative transfer equation (RTE), Eq. (1), given in section 3. This removes the assumption of a single-layer cloud with uniform extinction cross section, which was used in section 4 to derive infrared optical depth. HSRL data correctly provide an extinction cross section associated with the vertical temperature profile and, therefore, the emission throughout the cloud. The RTE is then solved in a forward calculation using the visible optical depth profile while iterating the visible-to-infrared optical depth ratio, $\alpha(\nu)$, until the forward solution matches the AERI-measured value at each microwindow. The infrared cloud transmissivity, as a function of cloud infrared optical depth, can then be described in terms of the scaled, HSRL-measured, visible cloud optical depth:

$$\tau_{\text{cld}}(\nu, p_t, p_b) = \exp[-\delta_{\text{IR}}(\nu, p_t, p_b)]$$
$$= \exp\left[\frac{-\delta_{\text{vis}}(p_t, p_b)}{\alpha(\nu)}\right]. \tag{12}$$

Using this information, the visible optical depth profile can be transformed into an infrared optical depth profile and substituted in Eq. (1), such that

$$R_m\downarrow \approx R_{\text{clr}}^{\text{LBL}}(p_s, p_b)\downarrow + r(\tau_{\text{cld}})\tau_{\text{clr}}^{\text{LBL}}(p_s, p_b)R_{\text{clr}}^{\text{LBL}}(p_s, p_b)\uparrow$$
$$+ \tau_{\text{clr}}^{\text{LBL}}(p_s, p_b)$$
$$\times \int_{p_t}^{p_b} B[\nu, T(p)]\, d\left\{\tau_{\text{clr}}(p, p_b)\exp\left[\frac{-\delta_{\text{vis}}(p, p_b)}{\alpha(\nu)}\right]\right\}, \tag{13}$$

where spectral dependence is once again implied. The right side of Eq. (13) is then solved in a forward calculation, while iterating $\alpha(\nu)$, until it agrees with the AERI-measured downwelling radiance, $R_m\downarrow$, to within 0.001 mW (m^2 sr cm^{-1})$^{-1}$. This is repeated for each spectral microwindow. Results are presented in section 7b.

7. Results

Data were acquired at the University of Wisconsin—Madison (96°N, 32°W) during simultaneous operation of the HSRL and AERI systems. Each case includes a local CLASS radiosonde launch. This section is broken into two subsections: 1) infrared optical depth results assuming uniform cloud extinction cross section (HSRL was used only for cloud-boundary information), and 2) visible-to-infrared optical depth ratio measurements using the HSRL-measured visible optical depth profile. For the latter approach, the results are compared to Mie theory to demonstrate sensitivity to particle size and shape.

Emphasis will be placed on data from two cases. Data from these days are useful in that the data acquisition period extended for several hours and the cirrus observations were over a range of optical thickness and cloud-base altitudes. HSRL-measured aerosol backscatter and depolarization for 17 November 1994 (hereafter case 1, Figs. 3a and 3b, respectively) and 9–10 November 1995 (hereafter case 2, Figs. 3c and 3d, respectively) are useful to gain a perspective on the atmospheric column scene and cloud phase. Times are given in universal coordinated time (UTC). The data are displayed in range-time-indicator (RTI) format, in which the scale is given to the right of each image. Large depolarization values show the clouds from both cases to consist entirely of ice particles. The planetary boundary layer is apparent in the bottom 2 km of each RTI.

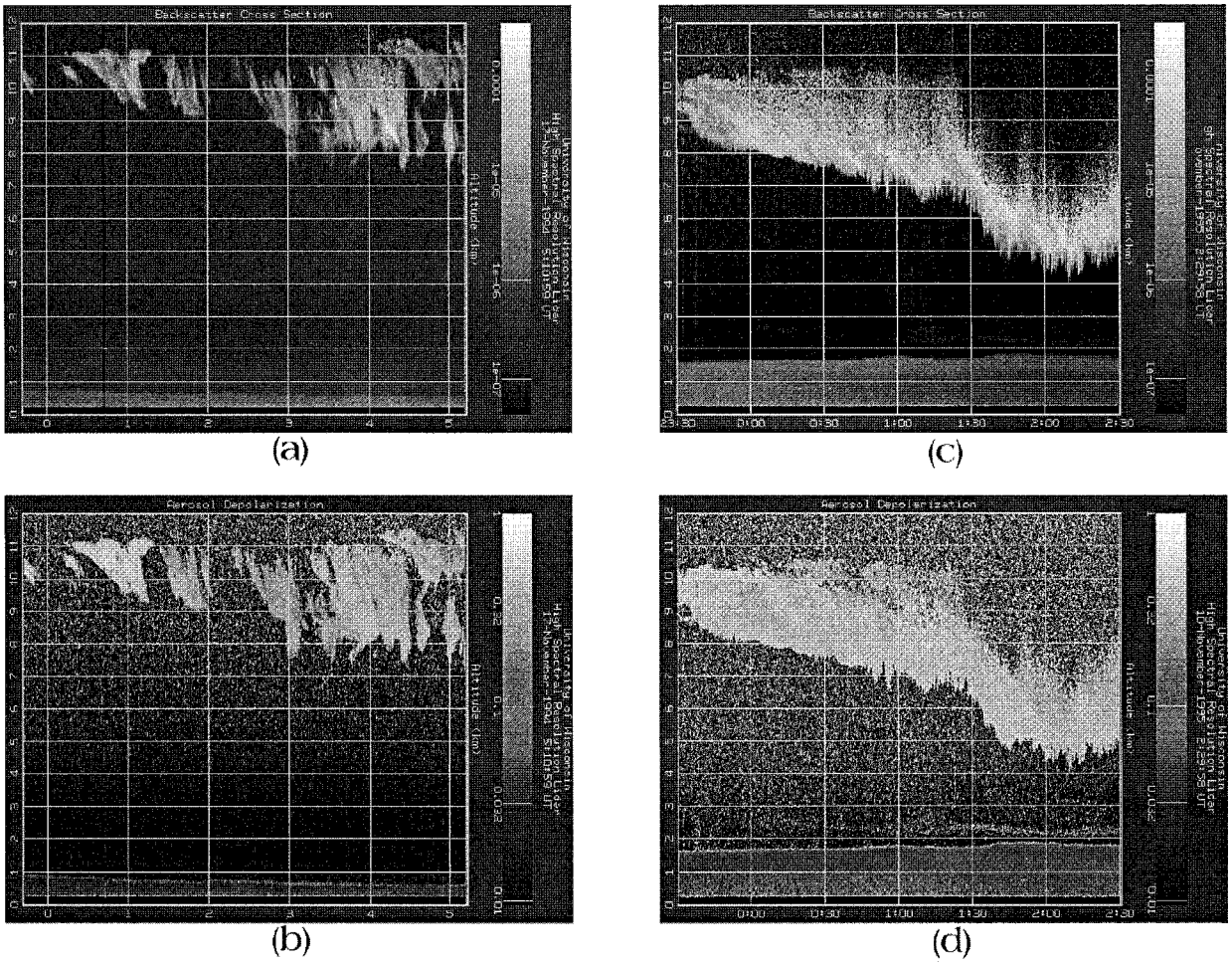

FIG. 3. [(a), (c)] HSRL-inverted aerosol backscatter and [(b), (d)] depolarization data. The abscissa indicates time in UTC format. Data are shown for 17 November 1994 [(a), (b)] and 9–10 November 1995 [(c), (d)].

a. Infrared spectral optical depth

The technique given in section 4 will be applied to data from the two cases shown in Fig. 3. This will produce cirrus cloud infrared optical depth as a function of time for each of the spectral microwindows listed in appendix A. The results assume a cloud of uniform extinction cross section within the lidar-measured cloud boundaries.

Case 1 was composed of broken cirrus located between 7 and 12 km for data acquired between 0000 and 0500 UTC. A radiosonde was released at 0006 UTC to obtain atmospheric-state information required to derive molecular emission using LBLRTM. Figure 4 illustrates cirrus cloud optical depth as a function of time for visible HSRL measurements (heavy black line) and each infrared microwindow (numerous gray lines). The visible and infrared optical depth data agree well in Fig. 4—aside from a few points that will be discussed next. The nearly 2:1 ratio between visible and infrared optical depths is expected from Babinet's principle (Hecht 1990). Deviation from this ratio is due to the absorption efficiency for ice that varies across the atmospheric window. This also explains the spread in microwindow data with increased optical depth. Visible-to-infrared optical depth results in section 7b will demonstrate this effect.

The visible data are included in Fig. 4 to show their correlation with the infrared data. Discrepancies occur near 0300 and 0500 UTC. HSRL visible data are obtained roughly every 3 s and are averaged over 3-min intervals to determine the optical depth. AERI infrared data are acquired over a 3-min dwell time but have a nearly 4-min dark period due to system calibration and data transfer. One obvious difference results when a sudden change in the cloud optical depth occurs over a short time period, as is apparent in Fig. 4. The AERI is in calibration mode at 0500 UTC and does not observe a large change in optical depth, which is measured by the HSRL.

AERI and HSRL FOV differences are also important in interpreting the data, whereas the HSRL FOV is 160 μrad, the AERI FOV is 32 mrad. This corresponds to an AERI-observed scene area that is more than four

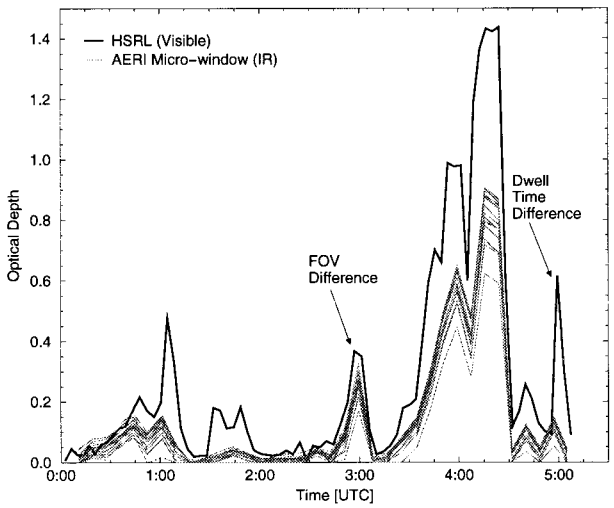

FIG. 4. HSRL visible and AERI infrared optical depth as a function of time on 17 November 1994. The numerous thin gray lines represent the various AERI microwindow regions. Note the spread in the microwindow lines as a result of the optical depth spectral dependence. Inconsistencies in the data near 0300 and 0500 UTC are a result of HSRL and AERI FOVs and dwell-time differences.

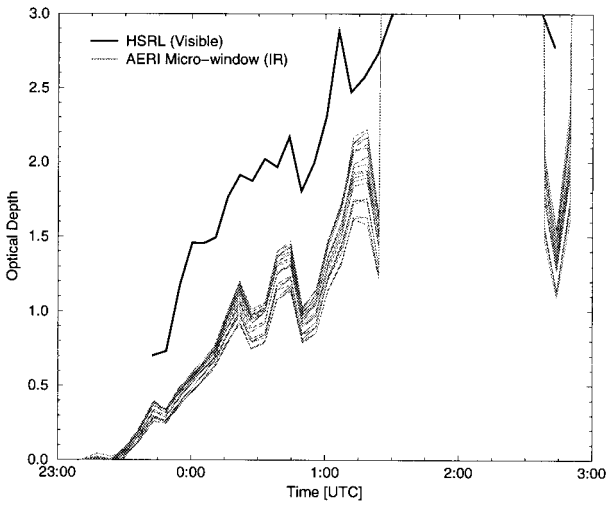

FIG. 5. Same as Fig. 4 but for data acquired during 9–10 November 1995. Note that the cloud becomes opaque between 0130 and 0230 UTC, as signified by an optical depth greater than 3.0.

orders of magnitude larger than the HSRL. The difference becomes significant for several conditions: 1) the HSRL is observing the edge of a cloud that is within the AERI FOV, 2) a small break in cloud cover occurs in the HSRL FOV but is not detectable within the larger AERI FOV, or 3) the HSRL FOV is clear but a small band of clouds is clipping the edge of the AERI FOV. Each of these cases would yield an AERI-measured optical depth that is larger than expected based on HSRL observations. Figure 4 illustrates a probable occurrence of this effect near 0300 UTC.

Case 2 was composed of overcast cirrus for data acquired between 2300 UTC 9 November 1995 and 0300 UTC 10 November 1995. Atmospheric-state data were acquired from a radiosonde released at 0057 UTC. The HSRL-measured cloud base decreased from 8.5 to 4.5 km in a period of 2 h, while the measured optical depth increased nearly monotonically until the cloud became opaque to the lidar. Optical depth data are shown in Fig. 5. Good data correlation exists, given the overcast conditions and nearly uniform increase in cloud optical depth. Note that the infrared optical depths become opaque near 0130 UTC, in agreement with the lidar measurements. Figure 6 illustrates optical depth as a function of cloud radiance for the 934-cm^{-1} microwindow, where the instrument has been projected to cloud base. The infrared optical depth gradually increases to a value of 1.6, where it then increases to 3.0 with an additional 25% increase in cloud radiance. Above this value, a 5% increase in cloud radiance yields a large increase in the optical depth. These calculations suggest that optical depth values above 3.0 are very uncertain. Clouds with infrared optical depths greater than 3.0 are considered to be opaque.

b. Visible-to-IR optical depth ratios

AERI and HSRL data are combined to derive the visible-to-infrared optical depth ratio, $\alpha(\nu)$, by iteration using the formalism discussed in section 6. The HSRL vertical aerosol optical depth profile effectively weights the radiosonde temperature profile when determining the cloud radiance. LBLRTM calculations provide a molecular optical depth profile from local radiosonde data. The aerosol optical depth profile is coupled with the molecular optical depth profile, and the RTE is solved in a forward calculation. Here, $\alpha(\nu)$ is iterated until the forward calculation agrees with measured results to within 0.001 mW $(m^2\ sr\ cm^{-1})^{-1}$. The process is repeated for each spectral microwindow radiance.

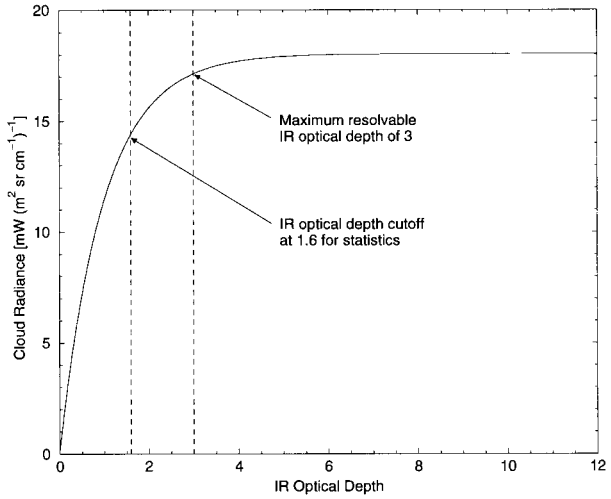

FIG. 6. Calculated infrared optical depth as a function of cloud radiance for 934 cm^{-1} microwindow. Small changes in cloud radiance yield a large increase in the cloud optical depth for infrared optical depths greater than 3.0, and the cloud is considered opaque.

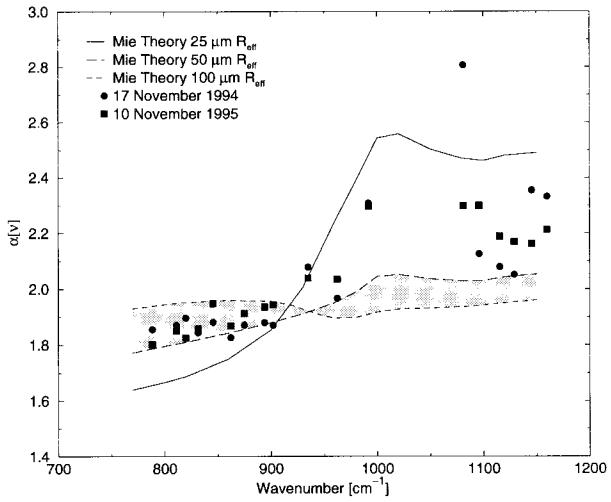

FIG. 7. Spectral visible-to-infrared optical depth data for 17 November 1994 and 10 November 1995. The shading represents particle sizes between 50- and 100-μm effective radius based on Mie calculations. A spectral bias relative to Mie theory indicates failure of Mie theory to properly represent $\alpha(\nu)$ in regions of weak absorption (950–1200 cm^{-1}), where there is strong sensitivity to both particle size and shape.

AERI and HSRL FOV and dwell-time differences were demonstrated by comparing HSRL-measured visible and AERI-derived infrared optical depths (Fig. 4). These differences will also apply to this data analysis, where slowly varying or uniform scene cirrus will provide better results than broken cloud cover conditions. A spectral comparison of $\alpha(\nu)$ data for cases 1 and 2 is given in Fig. 7 relative to calculations based on Mie theory assuming 25-, 50-, and 100-μm ice spheres. The Mie calculations were based on a gamma size distribution, where the theoretical $\alpha(\nu)$ was determined by comparing the ratio of visible scattering to infrared absorption coefficients.

Figure 7 illustrates that experimental values of $\alpha(\nu)$ for the two cases are consistent with Mie theory for 50–100-μm radius particles for wavenumbers smaller than 900 cm^{-1} and are consistent with 25–50-μm radius particles for wavenumbers larger than 900 cm^{-1}. The shading represents particle sizes between 50 and 100 μm. This suggests that the entire experimental curve is biased toward larger values of $\alpha(\nu)$ or that there is a spectral bias in the data relative to Mie calculations. Analysis of Eq. (13) indicates that there are four possible explanations for a potential bias in experimental data: 1) LBLRTM-calculated clear-sky radiance was overestimated, 2) AERI-measured downwelling column radiance was overestimated, 3) HSRL-measured cloud visible optical depth was overestimated, and 4) FOV differences between the instruments yield uncorrelated observations. A spectral bias could occur because of limitations in the Mie calculations while attempting to predict radiative properties of aspherical particles.

We will first consider a potential bias in the experimental data. The first two possibilities are inconsistent with instrumental characteristics and measured results. LBLRTM calculations within the microwindow regions slightly underestimate the radiance relative to AERI-measured values for humid conditions (i.e., this bias is in the wrong direction and the winter conditions were dry). The small uncertainty in the AERI measurements (Revercomb et al. 1996) eliminates the second possibility. HSRL measurement errors exist because of multiply-scattered return within the HSRL field of view. The effect of multiple scattering in the lidar return signal is difficult to measure and is dependent upon the chosen boundaries in the data analysis. Multiple scattering tends to underestimate the optical depth near cloud base and to overestimate the optical depth near cloud top (Eloranta and Piironen 1996). However, the total-column integrated optical depth value for the cloud remains correct if one integrates well beyond the cloud boundaries. Therefore, the measured total visible optical depth is correct, but the calculated radiance derived from the optical depth profile is skewed because the measured cloud extinction is spread over a distance greater than the cloud boundaries. This results in a reduced radiance, from the calculation, and an increased visible-to-infrared optical depth ratio. Thus, the first three possibilities are either negligible or produce a bias in the opposite direction.

AERI and HSRL instrumental differences are also likely to induce a bias in the $\alpha(\nu)$ results. FOV differences between the instruments were shown to account for large errors during nonuniform cloud cover cases. The results from case 1 (circles) exhibited greater scatter than case 2 (squares) in Fig. 7. This was expected given the nonuniformity in cloud cover and optical depth for broken cirrus. Aside from the additional scatter in case 1, there was no net bias between the two datasets, which one might expect for FOV errors associated with broken cloud cover.

Remotely sensed particle size measurements (Eloranta and Piironen 1996) were available for case 2, in which it was determined that the cloud consisted of 56-μm effective radius particles. These results are consistent with the data presented here relative to Mie theory—however, only in the spectral region of strong infrared absorption (800–900 cm^{-1}). Thus, there is evidence to conclude that a spectral bias exists in the experimental results relative to Mie theory. Strong lidar depolarization data in Fig. 3d show the cloud particles to be aspherical, which would support the disagreement with Mie theory. We can therefore conclude that Mie theory is effective for aspherical particles in regions of strong absorption (i.e., insensitive to particle shape). This also suggests that regions of weak absorption (950–1200 cm^{-1}) are very sensitive to particle shape, where the separation between the $\alpha(\nu)$ measurements and Mie theory calculations is due to the fact that we are comparing ice-sphere calculations to aspherical measurements. Takano et al. (1992) demonstrated particle-shape

TABLE A1. AERI microwindow regions.

Window	Start window (cm^{-1})	End window (cm^{-1})
1	785.917	790.739
2	809.061	812.919
3	815.330	824.491
4	828.348	834.617
5	842.814	848.118
6	860.172	864.030
7	872.227	877.531
8	891.996	895-853
9	898.264	905.497
10	929.606	939.731
11	959.983	964.323
12	985.056	998.075
13	1076.670	1084.867
14	1092.100	1098.850
15	1113.316	1116.691
16	1124.406	1132.603
17	1142.246	1148.032
18	1155.265	1163.462

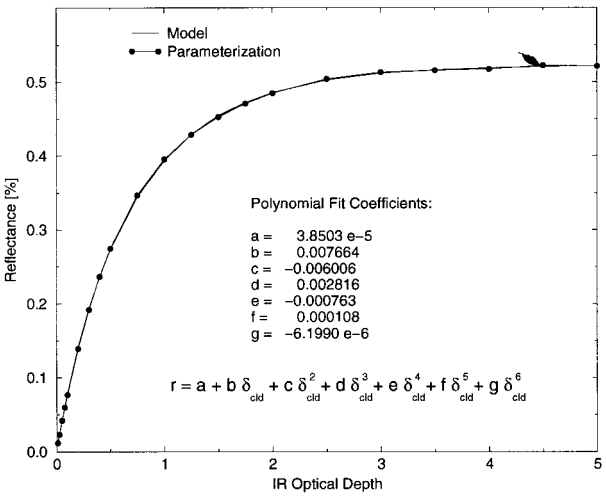

FIG. B1. Reflectance as a function of IR optical depth and a sixth-order polynomial fit for the microwindow region centered at 788 cm^{-1}. The fit is required to parameterize reflectance to allow optical depth inversion from the IR RTE.

insensitivity for strong absorption. One can also make this argument in terms of particle-size sensitivity (i.e., regions where Mie theory is sensitive to particle size would also be sensitive to particle shape). Results from Takano and Liou (1989) demonstrated that comparison of ice spheres to hexagons are different when assuming equivalent-area spheres versus equivalent-volume spheres. In this context, the region of strong absorption is proportional to the particle area, whereas the weak absorption is proportional to particle volume. Hence, the deviation from Mie theory increases with decreasing ice absorption.

8. Summary

Independent remote sensing at visible and infrared wavelengths, using ground-based HSRL and AERI, respectively, produced cirrus cloud optical depth measurements for Madison, Wisconsin. A series of 18 infrared microwindows, spectral regions between water vapor absorption lines, was compared to visible lidar measurements. Radiosonde data provide local atmospheric temperature and dewpoint temperature information. Clear-sky radiances were calculated using the LBLRTM model.

Infrared optical depths were measured from high spectral resolution AERI radiance measurements, where the cirrus cloud extinction cross section through the cloud was assumed to be uniform. Cloud boundaries were determined by lidar data such that this approach was not specific to the use of HSRL data. AERI-derived cirrus cloud infrared optical depths were compared to HSRL-measured visible optical depths to demonstrate the correlation between the instruments and potential sources of error due to instrument sampling frequency and FOV differences.

The spectral visible-to-infrared optical depth ratio, $\alpha(\nu)$, results were determined by using the HSRL-measured visible optical depth profile in the data analysis. The ratio was achieved by calculating the downwelling radiance using the HSRL visible optical depth divided by a visible-to-infrared optical depth ratio (i.e., assuming that the infrared optical depth was nearly monochromatic and linearly related to the HSRL-measured optical depth) with the optical depth ratio iterated until the calculated radiance matched the AERI-measured value. This procedure was repeated for each microwindow to yield a spectral comparison across the longwave infrared window.

The measurement of cirrus cloud infrared optical depths is a useful product to determine the impact of cirrus cloud cover on upwelling terrestrial radiation. However, including the HSRL visible optical depth profile to the dataset extends this data product. Visible-to-infrared optical depth ratios provide an effective cloud-forcing measurement, where downwelling solar radiation is represented by the visible lidar measurements. The latter approach also removed the assumption of a uniform extinction cross section in a single-layer cloud. These techniques can be extended to calculate the upwelling radiance, which would be measured by spaceborne instrumentation and applying a top-down solution of the radiative transfer equation, assuming the atmosphere does not become opaque due to optically thick cloud cover.

Results were presented for two cloud cases: 1) a broken and variable cirrus cloud cover example and 2) an overcast cirrus example with slowly varying optical thickness. The measured cirrus cloud visible-to-infrared optical depth ratios were compared to Mie theory, which demonstrated a spectral senstivity to both particle size and shape. The results indicated a spectral bias relative to the Mie calculations. It was concluded that this bias

TABLE B1. Reflectance fit coefficients.

Micro-window (cm^{-1})	$a \times 10^{-5}$	$b \times 10^{-3}$	$c \times 10^{-3}$	$d \times 10^{-3}$	$e \times 10^{-4}$	$f \times 10^{-4}$	$g \times 10^{-6}$
788	3.8503	7.6638	−6.0055	2.8156	−7.6313	1.0839	−6.1990
811	3.6348	7.1907	−5.6321	2.6428	−7.1704	1.0194	−5.8339
820	3.5399	6.9738	−5.4638	2.5656	−6.9656	0.9908	−5.6724
831	3.5093	6.6325	−5.2271	2.4700	−6.7406	0.9624	−5.5254
846	3.2853	6.1136	−4.8293	2.2878	−6.2555	0.8944	−5.1399
862	3.0069	5.4711	−4.3383	2.0628	−5.6558	0.8102	−4.6621
875	2.7645	4.9264	−3.9209	1.8710	−5.1439	0.7382	−4.2533
894	2.3410	3.9045	−3.1262	1.4978	−4.1250	0.5921	−3.4095
902	2.1395	3.4956	−2.8113	1.3524	−3.7352	0.5372	−3.0979
935	1.2622	1.8554	−1.5322	0.7510	−2.0987	0.3041	−1.7628
962	1.3547	1.9466	−1.6173	0.7948	−2.2233	0.3223	−1.8688
992	1.9235	2.8994	−2.3775	1.1578	−3.2208	0.4653	−2.6902
1081	2.4633	4.0218	−3.2373	1.5550	−4.2874	0.6158	−3.5472
1096	2.4832	4.0746	−3.2745	1.5712	−4.3288	0.6214	−3.5784
1115	2.5223	4.1853	−3.3529	1.6056	−4.4185	0.6338	−3.6486
1129	2.5462	4.2579	−3.4040	1.6281	−4.4778	0.6422	−3.6958
1145	2.5693	4.3299	−3.4540	1.6498	−4.5338	0.6499	−3.7389
1159	2.5818	4.3689	−3.4799	1.6607	−4.5613	0.6536	−3.7596

was not due to instrument FOV and sample frequency differences. A broken and quickly varying atmospheric scene (case 1) would exhibit a bias relative to a uniform atmospheric scene (case 2) if instrument temporal and spatial differences influenced the spectral bias (i.e., case 2 would show better agreement relative to Mie theory than case 1). Rather, case 1 showed greater scatter across the spectrum but was otherwise consistent with case 2. Mie theory assumptions were believed to underestimate (by roughly 10%) the visible-to-infrared optical depth ratio in regions of weak ice absorption (950–1200 cm^{-1}) but to agree with the results in regions of strong ice absorption (800–900 cm^{-1}). The spectral bias in the measured results relative to Mie theory occurred in the weak absorption region and was likely due to particle shape (i.e., strong absorption has small sensitivity to particle size and negligible sensitivity to particle shape; weak absorption has strong sensitivity to both particle size and shape). The data indicated particles on the order of 50-μm effective radius. It is expected that the shape sensitivity would increase with particle size, as the particles become increasingly aspherical. Analysis of ice crystals smaller than 25-μm effective radius needs to be performed for a general validation of the Mie theory ice-sphere results because there is observational evidence (Smith et al. 1998; Prabhakara et al. 1993) that extremely large spectral variation in the infrared optical depth is characteristic of very small particle ice clouds (e.g., subvisible cirrus and jet contrails).

Acknowledgments. Special thanks to Bob Knuteson and Hank Revercomb for their useful discussions regarding the AERI. Additional thanks to Andrew Collard for help and use of the adding–doubling model required to derive the cirrus cloud reflectance parameterizations. This work was partially supported through the Wisconsin Space Grant Consortium and the following grants: NSF, ATM-9321330; NASA, NAG-1-882; Lockheed, SK30G4160F; USAFGL, F19628-91-K-0007; NOAA, NA47EC0057; and DOE, DR-FG02-90ER61057.

APPENDIX A

AERI Microwindow Regions

A number of low-absorption regions exist between atmospheric absorption lines. These microwindows can be observed by the high spectral resolution of the AERI. They compose the least-absorbing regions within the spectral bandpass of the instrument. Refer to Table A1.

APPENDIX B

Cloud Reflectance Parameterization

A phase function can be determined from Mie theory if given the particle size distribution, particle phase, optical depth, and wavenumber. If a particle size distribution is assumed under natural cirrus conditions (ice clouds with an assumed effective radius near 50 μ) for a given microwindow region, the optical depth remains the only unknown.

Reflectance was calculated for a series of optical depths for each microwindow region, where the infrared optical depth varied from 0.01 to 5.0. The upper limit is beyond the capabilities of the lidar and is an acceptable cutoff.

Figure B1 shows a plot of reflectance as a function of the infrared optical depth that is subsequently fit with a sixth-order polynomial to determine a parameterization for the reflectance for the given optical depth range. Data shown are at 772 cm^{-1}. The calculated reflectance for the given assumptions varies from 0% to 0.52%, among all microwindows.

The coefficients for each microwindow region are given in Table B1, such that

$$r(\delta_{\text{cld}}) = a + b\delta_{\text{cld}} + c\delta_{\text{cld}}^2 + d\delta_{\text{cld}}^3 + e\delta_{\text{cld}}^4 + f\delta_{\text{cld}}^5 + g\delta_{\text{cld}}^6,$$

where the reflectance is valid for infrared optical depths between 0 and 5, and the spectral dependence is implied.

REFERENCES

Ackerman, S. A., W. L. Smith, J. D. Spinhirne, and H. E. Revercomb, 1990: The 27–28 October 1986 FIRE IFO cirrus case study: Spectral properties of cirrus clouds in the 8–12-μm window. *Mon. Wea. Rev.*, **118,** 2377–2388.

——, E. W. Eloranta, C. J. Grund, R. O. Knuteson, H. E. Revercomb, W. L. Smith, and D. P. Wylie, 1993: University of Wisconsin remote sensing pilot experiment. *Bull. Amer. Meteor. Soc.*, **74,** 1041–1049.

Chappelaz, J., T. Blunler, D. Reynaud, J. M. Barnola, J. Schwander, and B. Stauffer, 1993: Synchronous changes in atmospheric CH_4 and Greenland climate between 40 and 8 kyr BP. *Nature*, **366,** 443–445.

Clough, S. A., M. J. Iacono, and J.-L. Moncet, 1992: Line-by-line calculation of atmospheric fluxes and cooling rates: Application to water vapor. *J. Geophys. Res.*, **97,** 15 761–15 785.

Collard, A. D., S. A. Ackerman, W. L. Smith, X. Ma, H. E. Revercomb, R. O. Knuteson, and S.-C. Lee, 1995: Cirrus cloud properties derived from high spectral resolution infrared spectrometry during FIRE II. Part II: Ground-based HIS results. *J. Atmos. Sci.*, **52,** 4264–4275.

Eloranta, E. W., 1998: A practical model for multiply scattered lidar return. *Appl. Opt.*, **37,** 2464–2472.

——, and P. Piironen, 1996: Measurements of particle size in cirrus clouds with the high spectral resolution lidar. *Eighth Int. Workshop on Multiple Scattering Lidar Experiments.* Quebec, PQ, Canada, MUSCLE8, 98–101.

Francis, P. N., 1995: Some aircraft observations of the scattering properties of ice crystals. *J. Atmos. Sci.*, **52,** 1142–1154.

Genthon, C., J. M. Barnola, D. Reynaud, C. Lewis, J. Jouzel, N. I. Barkov, Y. S. Kotkevich, and V. M. Kotlyakov, 1987: Vostok ice core: Climatic response to CO_2 and orbital forcing changes over the last climatic cycle. *Nature*, **366,** 414–418.

Grund, C. J., and E. W. Eloranta, 1991: University of Wisconsin high spectral resolution lidar. *Opt. Eng.*, **30,** 6–12.

Hansen, J. E., 1971: Multiple scattering of polarized light in a planetary atmosphere. Part II: Sunlight reflected by terrestrial water clouds. *J. Atmos. Sci.*, **28,** 1400–1426.

Hecht, E., 1990. *Optics.* Addison-Wesley, 676 pp.

Measures, R. M., 1992: *Laser Remote Sensing: Fundamentals and Applications.* Krieger, 42 pp.

Piironen, P., 1994: A high spectral resolution lidar based on an iodine absorption filter. Ph.D. thesis, University of Joensuu, Finland, 113 pp. [Available from Joensuu University Library, Sale of Publications, P.O. Box 107, FIN-80101 JOENSUU.]

——, and E. W. Eloranta, 1994: Demonstration of a high-spectral-resolution lidar based on an iodine absorption filter. *Opt. Lett.*, **19,** 234–236.

Platt, C. M. R., 1973: Lidar and radiometric observations of cirrus clouds. *J. Atmos. Sci.*, **30,** 1191–1204.

Prabhakara, C., D. P. Kratz, J.-M. Yoo, G. Dalu, and V. Vernekar, 1993: Optically thin cirrus clouds: Radiative impact on the warm pool. *J. Quant. Spectrosc. Radiat. Transfer*, **49,** 467–483.

Revercomb, H. E., and Coauthors, 1996: Atmospheric emitted radiance interferometer (AERI), Part I: Status, basic radiometric accuracy, and unexpected errors and solutions. *Proc. Sixth Atmospheric Radiation Measurement (ARM) Science Team Meeting*, San Antonio, TX, 273–277.

Rossow, W. B., and A. A. Lacis, 1990: Global, seasonal cloud variations from satellite radiance measurements. Part II: Cloud properties and radiative effects. *J. Climate*, **3,** 1204–1253.

Schneider, S. H., 1990: The global warming debate heats up: An analysis and perspective. *Bull. Amer. Meteor. Soc.*, **71,** 1292–1304.

Smith, W. L., H. E. Revercomb, R. O. Knuteson, F. A. Best, R. Dedecker, H. B. Howell, and H. M. Woolf, 1995: Cirrus cloud properties derived from high spectral resolution infrared spectrometry during FIRE II. Part I: The high resolution interferometer sounder (HIS) systems. *J. Atmos. Sci.*, **52,** 4238–4245.

——, S. Ackerman, H. Revercomb, H. Huang, D. H. DeSlover, W. Feltz, L. Gumley, and A. Collard, 1998: Infrared spectral absorption of nearly invisible cirrus clouds. *Geophys. Res. Lett.*, **25,** 1137–1140.

Takano, Y., and K.-N. Liou, 1989: Solar radiative transfer in cirrus clouds. Part I: Single-scattering and optical properties of hexagonal ice crystals. *J. Atmos. Sci.*, **46,** 3–19.

——, ——, and P. Minnis, 1992: The effects of small ice crystals on cirrus infrared radiative properties. *J. Atmos. Sci.*, **49,** 1487–1493.

Warren, S. G., 1984: Optical constants of ice from the ultraviolet to the microwave. *Appl. Opt.*, **23,** 1206–1225.